Functionalized hexagonal boron nitride nanoplatelets for advanced cementitious nanocomposites

Panagiotis A. Danoglidis, Cory M. Thomas, Myrsini E. Maglogianni, Mark C. Hersam, Maria S. Konsta-Gdoutos

PII: S0958-9465(23)00201-9

DOI: https://doi.org/10.1016/j.cemconcomp.2023.105127

Reference: CECO 105127

To appear in: Cement and Concrete Composites

Received Date: 25 January 2023

Revised Date: 4 May 2023 Accepted Date: 9 May 2023

Please cite this article as: P.A. Danoglidis, C.M. Thomas, M.E. Maglogianni, M.C. Hersam, M.S. Konsta-Gdoutos, Functionalized hexagonal boron nitride nanoplatelets for advanced cementitious nanocomposites, *Cement and Concrete Composites* (2023), doi: https://doi.org/10.1016/j.cemconcomp.2023.105127.

This is a PDF file of an article that has undergone enhancements after acceptance, such as the addition of a cover page and metadata, and formatting for readability, but it is not yet the definitive version of record. This version will undergo additional copyediting, typesetting and review before it is published in its final form, but we are providing this version to give early visibility of the article. Please note that, during the production process, errors may be discovered which could affect the content, and all legal disclaimers that apply to the journal pertain.

© 2023 Published by Elsevier Ltd.



Functionalized Hexagonal Boron Nitride Nanoplatelets

for Advanced Cementitious Nanocomposites

- Panagiotis A. Danoglidis ^a, Cory M. Thomas ^b, Myrsini E. Maglogianni ^a, Mark C. Hersam ^c and
- 4 Maria S. Konsta-Gdoutos^a1

1

2

- ^a Center for Advanced Construction Materials, Department of Civil Engineering, The University of Texas at Arlington, Arlington, TX 76019
- 8 b Department of Materials Science and Engineering, Northwestern University, Evanston, IL 60208
- 9 °Department of Materials Science and Engineering, Department of Chemistry, and Department of Electrical and
- 10 Computer Engineering, Northwestern University, Evanston, IL 60208

11 Abstract

- 12 Portland cement-based nanocomposites were successfully fabricated with low volume
- 13 fractions of hexagonal boron nitride (hBN) nanoplatelets, exfoliated and functionalized using
- 14 a combination of ball milling and sonicated-assisted dispersion. Surface topography, thickness,
- lateral dimension, and number of layers of the hBN nanoplatelets were evaluated by AFM and
- Raman analysis. The identification of functional groups attached onto the functionalized hBN
- was performed through FTIR. The results show that the functionalization successfully
- exfoliates the hBN nanoplatelets to few-layer thicknesses, resulting in suspensions with high
- 19 colloidal stability. The grafted hydroxyl and carboxyl groups on the hBN surface interact with
- 20 the Ca²⁺ ions of calcium silicate hydrates (CSH), improving the load-transfer efficiency from
- 21 the cement matrix to the hBN nanoplatelets. Overall, the hBN reinforced cementitious
- 22 composites demonstrated significant enhancement in flexural strength by ~50%, compressive
- strength by $\sim 17\%$, Young's modulus by $\sim 56\%$, and fracture energy by $\sim 76\%$.

24 Keywords

- 25 Hexagonal Boron Nitride, Exfoliation, Surface Functionalization, Number of layers, Modulus
- of Elasticity

27

Email address: <u>maria.konsta@uta.edu</u> (M.S. Konsta-Gdoutos)

¹ Corresponding author

28 Nomenclature

29 Symbols

2D Two-Dimensional

 σ_c Compressive Strength

 σ_f Flexural Strength

G_f Fracture Energy

 ζ Zeta potential

E Young's Modulus

I_{B-N} Intensity Ratio of Boron-Nitrogen Bonding

Ioh Intensity Ratio of Hydroxyl Groups

Number of Layers

30

31 Acronyms

AFM Atomic Force Microscopy

C-S-H Calcium Silicate Hydrates

CVD Chemical Vapor Deposition

FWHM Full-Width at Half-Maximum

FTIR Fourier Transform Infrared

hBN Hexagonal Boron Nitride

hBN-AR "As received" bulk Hexagonal Boron Nitride

hBN-BM Ball milled Hexagonal Boron Nitride

hBN-BM-U Ball milled Hexagonal Boron Nitride after ultrasonication

hBN-BM-U_{SFC} Ball milled Hexagonal Boron Nitride after ultrasonication with the use

of surfactant (SFC)

hBN-U Bulk Hexagonal Boron Nitride after ultrasonication

hBN-U_{SFC} Bulk Hexagonal Boron Nitride after ultrasonication with the use of

surfactant (SFC)

OPC ordinary Portland cement

SFC Surfactant

UV-vis Ultraviolet-Visible

CMOD Crack Mouth Opening Displacement

LEFM Linear Elastic Fracture Mechanics

Introduction

33

34

35

36

37

38

39

40

41

42

43

44

45

46

47

48

49

50

51

52

53

54

55

56

57

Recently, two-dimensional (2D) nanomaterials have demonstrated outstanding potential as reinforcing materials for high-performance nanocomposites. Hexagonal boron nitride (hBN), a dielectric isomorph of graphene, has drawn attention due to its unique combination of high intrinsic thermal conductivity and stability [1], electrically insulating behavior [2], and extraordinary mechanical properties including a Young's modulus of ~1 TPa [3]. Chemical functionalization can further enhance the synergistic advantages of few-layer hBN nanoplatelets [4-5]. Various physical and chemical methods have been reported to exfoliate hBN nanoplatelets including ball milling [6-8], intercalation-oxidation [9], chemical vapor deposition (CVD) [10], and liquid exfoliation [11-19]. Among these methods, sodium hydroxide (NaOH)-assisted ball milling has been found to be effective at functionalizing hBN nanoplatelets without significantly disrupting the crystal structure of the hBN [7]. In previous work from our laboratory, we have shown that functionalized hBN can improve gelation with ionic liquids, resulting in concurrently high ionic conductivity and mechanical stiffness, which is of high interest for rechargeable battery applications [20]. Similarly, functionalized hBN can improve interactions with polymer matrices to impart high thermal conductivity and stability, modulus of elasticity, and ionic conductivity, which have been successfully employed as separators between the cathode and anode electrodes in battery assemblies [21]. This prior work suggests that functionalized hBN can add value to additional nanocomposite materials. A couple previous attempts have been made to implement hBN nanoplatelets in cementitious matrices. For example, Rafiee et al. [22] employed high volumes (≈2.0 vol%) of ball-milled hBN nanosheets to increase the low compressive strength and toughness of porous cementitious composites. Another recent study reported the effectiveness of ultrasonication for enhancing the exfoliation state and colloidal stability of hBN nanosheets in suspension, which is crucial for enhancing the mechanical properties of hBN-reinforced cementitious materials

- 58 [19]. In this work, ultraviolet-visible (UV-vis) optical absorption spectroscopy indicated the
- 59 necessity of using surfactants to maintain the colloidal stability of the hBN suspensions.
- Herein, functionalized hBN nanoplatelets were produced from bulk hBN powders. A two-step
- 61 method was implemented to synergistically functionalize and exfoliate the hBN nanoplatelets
- 62 using ball milling and sonication. The functionalization degree was quantitatively assessed by
- evaluating the intensity ratio of hydroxyl groups (I_{OH}) to boron-nitrogen (I_{B-N}) bonding through
- 64 Fourier transform infrared (FTIR) spectroscopy. In addition, atomic force microscopy (AFM),
- Raman analysis, and zeta potential measurements were used to determine the number of hBN
- layers, thickness, lateral dimension, and charge transfer kinetic rates of the hBN nanoplatelets
- after exfoliation. An important first reporting step of this ongoing research is the impact of the
- degree of hBN's functionalization and exfoliation on the strength, stiffness and fracture energy
- of hBN-reinforced cementitious composites. The functionalized hBN nanoplatelets were
- 70 employed in cementitious nanocomposites, resulting in significant enhancement of flexural
- strength by \sim 50%, compressive strength by \sim 17%, Young's modulus by \sim 56%, and fracture
- 72 energy by \sim 76%.

2. Materials and Experimental Procedure

- 74 2.1 Materials and Specimen Preparation
- A ball milling process was used to produce hBN nanoplatelets from "as-received" bulk hBN
- 76 (hBN-AR) [7]. 8 g of bulk hBN (Sigma Aldrich, 1 μm) was mixed with 120 g of 2 M NaOH
- and 400 g of stainless-steel balls (6 mm) in a 150 mL stainless-steel ball milling container. The
- 78 mixture was ball milled (Micronano Tools, PBM-2) at 200 rpm for 24 h before the NaOH
- solution was filtered, and the recovered powder was bath sonicated with 300 mL of 1 M HCl
- 80 solution. The resulting slurry was filtered and washed with deionized water until the pH was
- 81 neutral. The powder was then dispersed in isopropyl alcohol at a concentration of 2 mg/mL via

82	bath sonication, after which the dispersion was centrifuged (Beckman Coulter, JLA-16.250) at
83	5,000 rpm before the supernatant was decanted. The supernatant was then filtered to collect the
84	functionalized hBN nanoplatelets (hBN-BM).
85	As-received bulk hBN (hBN-AR) and ball-milled hydroxylated hBN (hBN-BM) at a volume
86	fraction of 0.18 vol% were used to produce aqueous suspensions using a sonication-assisted
87	dispersion method. In particular, a previously reported one-step ultrasonication procedure that
88	employs a commercially available polycarboxylate based surfactant [23-25] was implemented
89	to further assist the hydroxylation and exfoliation and promote dispersion of the hBN samples
90	in water. Ultrasonication energy was applied to the aqueous samples using a 750 W cup-horn
91	high-intensity ultrasonic processor with a 19 mm diameter probe. Using the developed
92	dispersion method, the effect of the addition of the surfactant, at a fixed surfactant to hBN ratio,
93	on the stability of the hBN suspensions was evaluated. It should be noted that the 0.18 vol%
94	hBN loading was selected as the optimum volume fraction used to maximize the mechanical
95	and thermal properties of hBN reinforced epoxy nanocomposites [26].
96	Type I ordinary Portland cement (OPC) was used as the binding material. Standard sand as per
97	the ASTM C778-17 was used as the fine aggregate for casting mortars with water to cement
98	ratio of 0.485 and sand to cement ratio of 2.75. The hBN-AR and hBN-BM suspensions were
99	added to OPC and sand, with the subsequent mixing being performed according to the
100	procedure outlined by ASTM $305-20$ using a standard robust mixer capable of operating from
101	140 ± 5 rpm to 285 ± 10 rpm. The mixture was then cast in $40 \times 40 \times 160$ mm ³ oiled molds.
102	After 24 hours of curing, specimens were demolded and stored in a curing room (20 °C, 99.5%
103	humidity) until testing.

105	2.2 Characterization Methods
106	An AFM operating in tapping mode was used to measure the thickness and lateral size of the
107	hBN nanoplatelets following deposition onto silicon substrates under ambient conditions.
108	Information regarding the morphology of the sample was obtained using the height sensor with
109	ScanAsyst tips with a nominal radius of 2 nm. The spring constant of the AFM cantilevers was
110	$0.4\ \mathrm{N/m}$, and the scan rate was $0.5\ \mathrm{Hz}$. The peak amplitude was fixed at $150\ \mathrm{nm}$, and data from
111	256 points were collected along both the horizontal and vertical axes.
112	FTIR spectroscopy was performed to identify the functional groups on the hBN nanoplatelets.
113	The experiments were performed with 32 scans at a resolution of 4 cm ⁻¹ ranging from 4000 to
114	525 cm ⁻¹ . An ambient background scan was taken before each sample acquisition. 0.05 g of
115	hBN (powder) was used to obtain the FTIR spectra. Raman spectroscopy was carried out with
116	a 532 nm excitation laser in air under ambient conditions. 0.05g of hBN (powder) was used to
117	obtain the Raman spectra. After averaging, the spectra were baseline corrected in the region
118	1300–1440 cm ⁻¹ and peaks were fit to Lorentzians. For the hBN dispersions, the samples were
119	capped loosely and kept in an oven at 50 °C until the water was evaporated. Then, the dry hBN
120	samples were collected and FTIR and Raman analyses were performed.
121	Zeta potential measurements were used to evaluate colloidal stability of the suspensions and
122	the level of charge attraction/repulsion between the hBN nanoplatelets [27]. The zeta potential
123	was determined by measuring the electrophoretic mobility of the suspensions using the
124	Zetasizer Nano ZS system. Prior to electrophoretic mobility measurements, all samples were
125	diluted in distilled water at a constant factor. Following dilution, 1.0 ml of each sample was
126	loaded into a Malvern DTS 1070 disposable folded capillary cells to perform the zeta potential
127	measurements as per the instructions of the Zetasizer Nano ZS system manufacturer. The zeta
128	potential (ζ) was then calculated by the Helmotz-Smoluchowski equation:

$$\zeta = \mu \left(\frac{4\pi\eta}{\varepsilon}\right) \tag{1}$$

- where μ is the electrophoretic mobility, η is the viscosity of the dispersion medium (water =
- 131 0.8904 cp), and ε is the dielectric constant of the solvent (water = 78.54).
- 132 An isothermal conduction calorimeter was used to measure the heat of hydration of freshly
- mixed cement paste samples with a w/c of 0.485. The raw materials were pre-conditioned at a
- temperature of 23°C and then mixed thoroughly inside the vial at a speed of 200 ± 10 r/min for
- 135 180 s, in accordance with the ASTM C1679-17. Readings were recorded for every 15 sec
- during the first hour of hydration, and then for every 1 min until 40 hours of hydration period.
- 137 Three-point bending tests were conducted to assess the flexural strength of the cementitious
- nanocomposites. $4 \times 4 \times 16$ cm³ prismatic specimens were tested in three-point bending at the
- age of 3, 7, and 28 days according to ASTM C348-21. The test was performed using a 30 kN
- 140 MTS Criterion Electromechanical Testing system under displacement control. The rate of
- displacement was held constant at 0.1 mm/min [28]. An average value was calculated from
- three specimens for each curing age.
- 143 The compressive strength of the hBN reinforced mortars was determined on the two halves of
- the prism that resulted from the fracture of the three-point bending specimen according to
- 145 ASTM C349-18. Prior to subjecting them to a uniaxial compression test, the two halves were
- examined for the presence of cracks that might have been generated during the three-point
- bending test. The test was performed using a 500 kN MTS Servohydraulic Testing system
- under displacement control. The rate of displacement was held constant at 0.3 mm/s.
- The Young's modulus, E, was calculated from 2 different experimental procedures. First, the
- 150 Young's modulus was determined from the stress strain curves of the uniaxial compression
- tests following the ASTM C 469/C469M-14. The Young's modulus was also calculated by the

152	three point bending experiments following the ACI 544 Report on Fiber Reinforced Concrete
153	[28-29].
154	According to ASTM C348, ASTM C349 and ASTM C469 specimens that result in strengths
155	differing by more than 10% from the average value of all test specimens made from the same
156	sample and tested at the same period were not considered in determining the flexural and
157	compressive strength, and the modulus of elasticity.
158	Furthermore, fracture mechanics tests on notched $10 \times 10 \times 84 \text{ cm}^3$ specimens were employed
159	to evaluate the fracture energy, G_f , following the Linear Elastic Fracture Mechanics according
160	to the RILEM FMC-50 [30]. A 42 cm notch was introduced into the prismatic specimens using
161	a water-cooled band saw machine. The length of the notch was calculated based on the RILEM
162	standard which requires a notch a notch to depth ratio of close to 1/2 [30]. The specimens were
163	then tested at the age of 28 d, following the aforementioned three point bending procedure. The
164	test was performed using the 30 kN MTS Electromechanical Testing system. A Crack Mouth
165	Opening Displacement (CMOD) extensometer was used as the feedback signal to produce
166	stable crack propagation at the rate of 0.015 mm/sec, is reached about 1 min.
167	The microstructural analysis of the samples was carried out using a Scanning Electron
168	Microscopy (SEM) system Hitachi SU 3800 operating in in high vacuum mode. Prior to SEM,
169	the sample was sputter-coated with a thin layer of gold-platinum, Au/Pt, to eliminate charging
170	effects. The acceleration voltage was kept at 7.5 kV and spot size of 12.5 was considered for
171	SEM operations.
172	

3. Results and Discussion

175	3.1 hBN Functionalization, Exfoliation, and Stability
176	Representative AFM images for the hBN-AR and hBN-BM samples both before and after
177	ultrasonication are displayed in Figure 1. Figure 1a shows the hBN-AR sample in water having
178	lateral particle sizes in the range of 1-10 μm and thicknesses up to 120 nm. It should be noted
179	that the AFM-measured thickness of monolayer hBN has been previously reported in the
180	literature as \sim 1 nm [31]. The measured thickness for the hBN-AR suspension is about 2.4 times
181	higher than that of hBN bulk material, indicating the presence of agglomerated hBN particles.
182	hBN-BM was observed to have a thickness of ~63 nm, which is lower than that of hBN-AR.
183	After ultrasonication, the thickness of the hBN nanoplatelets was further reduced. In particular,
184	ultrasonication of the hBN-AR sample (i.e., hBN-U sample) results in a thickness of ~8 nm.
185	The lowest average thickness of ~5 nm was observed for the hBN-BM sample after
186	ultrasonication (i.e., hBN-BM-U) with some hBN-BM-U nanoplatelets being as thin as 3-4
187	layers.

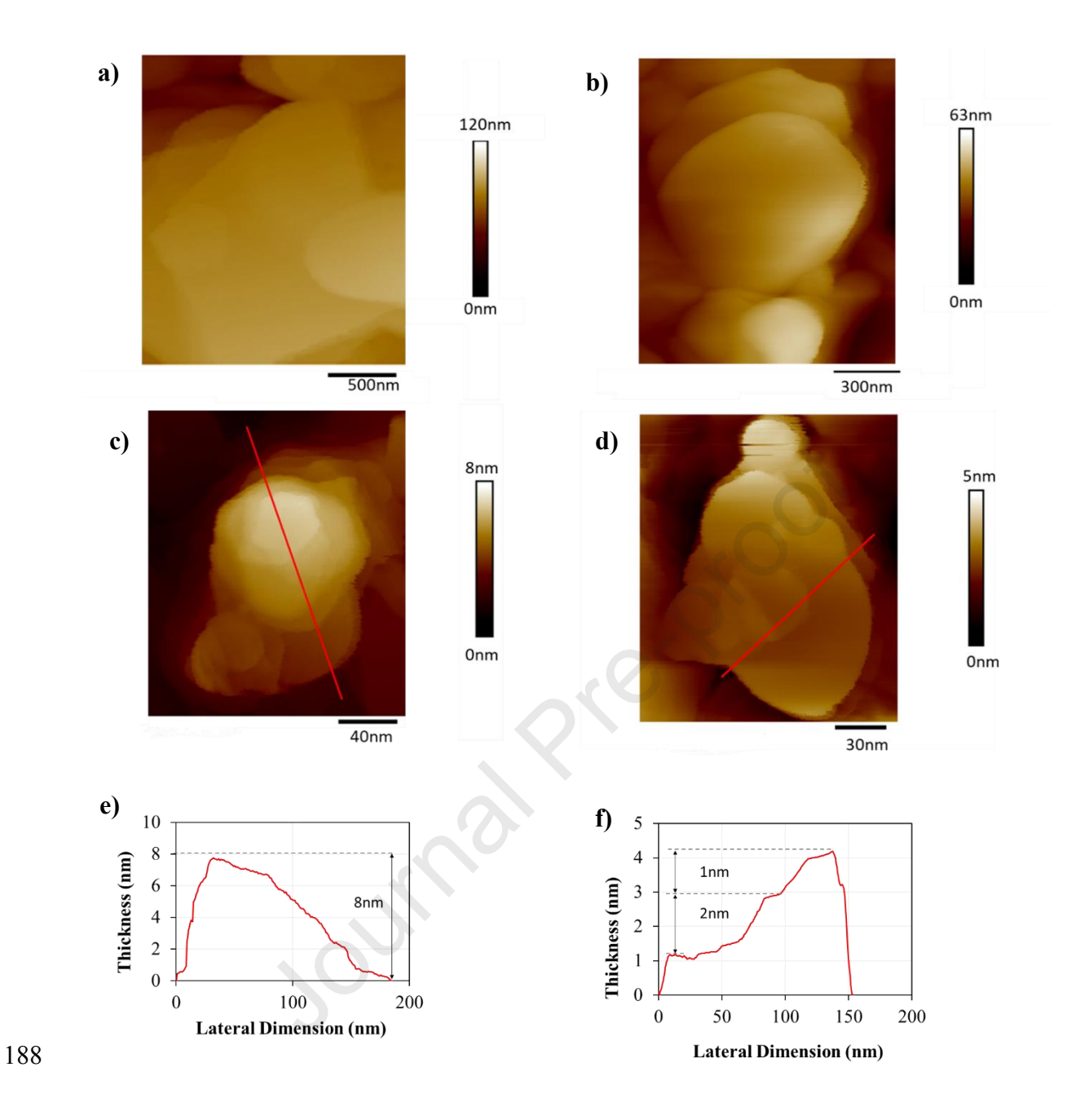
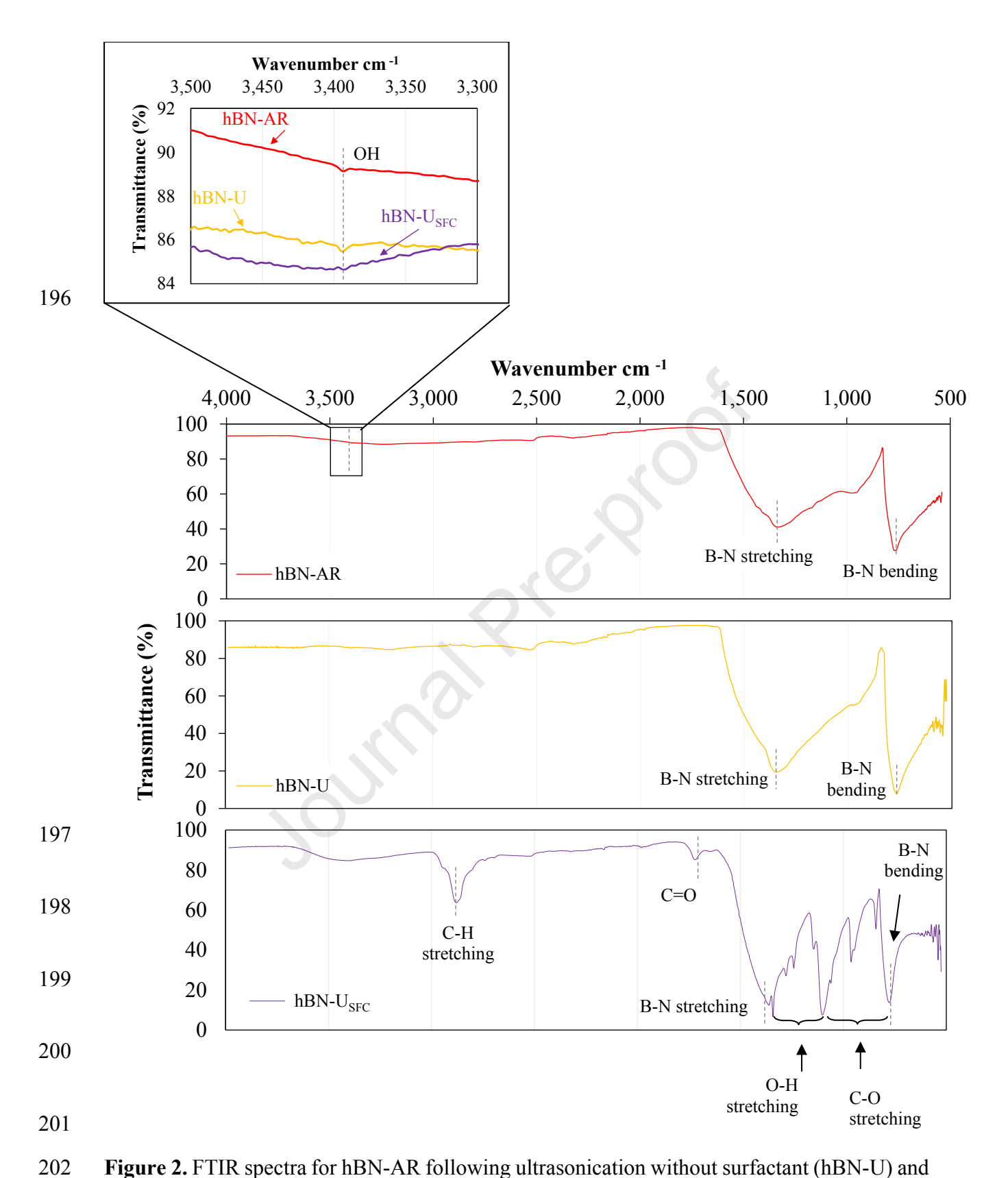


Figure 1. (a-d) AFM images of (a) hBN-AR, (b) hBN-BM, (c) hBN-U, and (d) hBN-BM-U. (e) Cross-sectional profile of the thickness along the line indicated in (c). (f) Cross-sectional profile of the thickness along the line indicated in (d).



 $\label{eq:Figure 2.} \textbf{FTIR spectra for hBN-AR following ultrasonication without surfactant (hBN-U) and with surfactant (hBN-U_{SFC}).}$

Figure 2 compares the FTIR spectra of the hBN-AR and hBN-U samples with and without
surfactants. The two characteristic absorption peaks of hBN at about 1340 and 770 cm ⁻¹ are
assigned to the stretching vibration of the B-N bond (in-plane) and bending vibration of B-N-
B (out-of-plane) [32], respectively, and are observed in the FTIR spectra of all hBN samples.
The presence of the two characteristic peaks around 1340 and 770 cm ⁻¹ confirms that the hBN
lattice remains intact after the application of ultrasonication energy for both the samples with
(hBN-UsFc) and without surfactants (hBN-U). The weak peak observed at \sim 3393 cm ⁻¹ (shown
in the insert of the figure for all hBN samples) is attributed to the stretching vibration of
hydroxyl groups (-OH) on the hBN surface. The peak at ~2520 cm ⁻¹ is likely resulting from
B-H bonds [33]. The absence of new peaks for the hBN-U spectra confirms that there are no
additional functional groups induced during the ultrasonication procedure. Two additional
peaks can be observed in the hBN-U _{SFC} spectra at wavenumbers near 2870 and 1710 cm ⁻¹ ,
which are attributed to the C-H and -COOH stretching vibrations. These additional peaks along
with the O-H stretching of carboxylate groups and C-O stretching at wavenumbers between
1340 and 816 cm ⁻¹ suggest that the use of surfactants during the ultrasonication procedure
(hBN-U _{SFC}) resulted in functionalization with carboxyl groups. In addition, a shift towards
higher wavenumber was observed for the two characteristic hBN peaks (Table 1) of the hBN-
U and hBN-U _{SFC} spectra, indicating that exfoliation of hBN enhances the stretching vibration
and especially bending vibration of B–N bonds [34]. Overall, these results show the importance
of adding surfactants to the ultrasonicated suspensions for improving the exfoliation and
functionalization of the hBN nanoplatelets

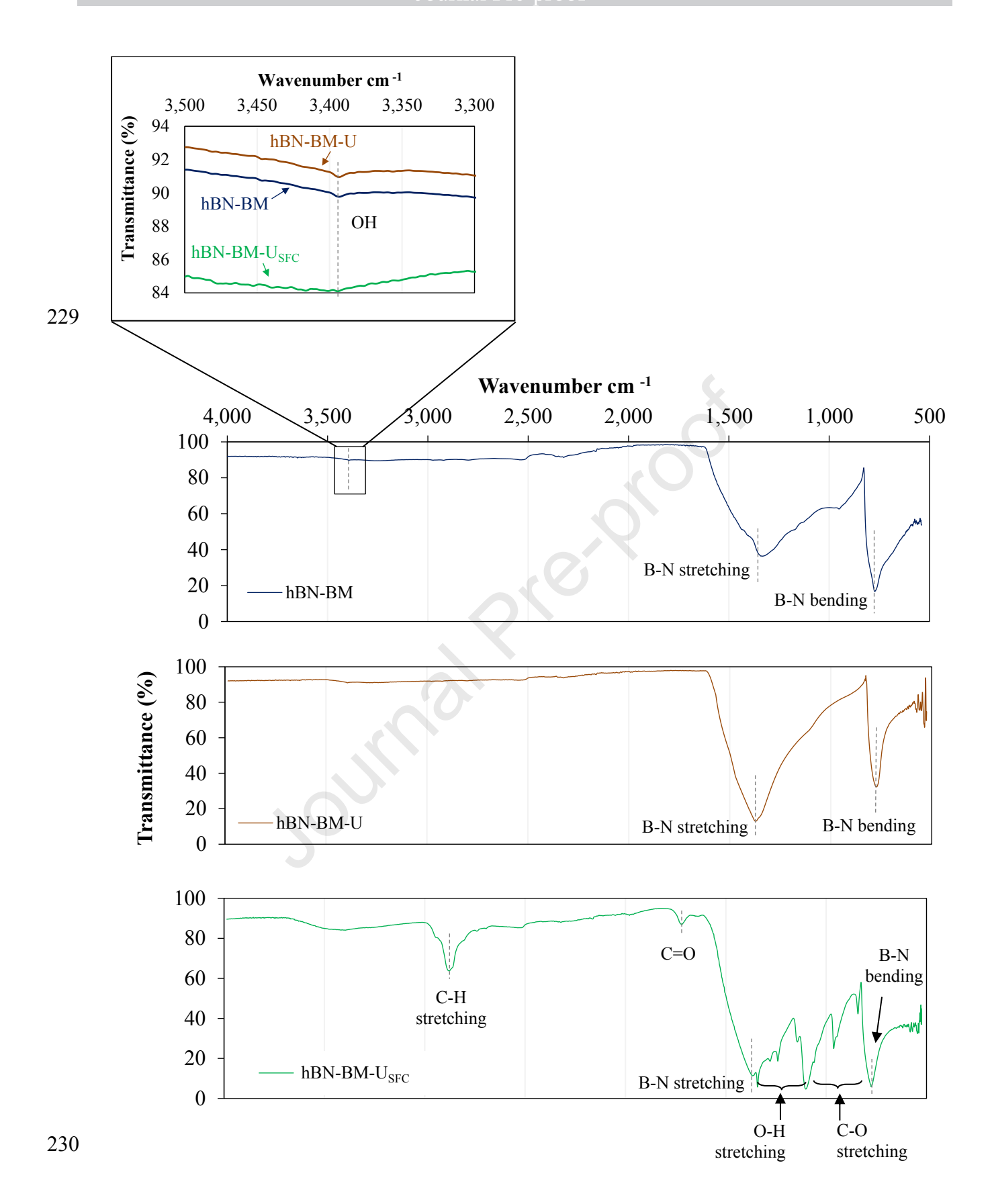


Figure 3. FTIR spectra for hBN-BM following ultrasonication without surfactant (hBN-BM-U) and with surfactant (hBN-BM-U_{SFC}).

Figure 3 compares the FTIR spectra of the hBN-BM and hBN-BM-U samples with and without
surfactants (i.e., hBN-BM-U _{SFC} and hBN-BM-U, respectively). Compared to hBN-AR, hBN-
BM does not exhibit any additional peaks in the FTIR spectra, which indicates that there are
no deleterious functional groups grafted onto the hBN surface during ball milling. Comparing
the FTIR spectra of hBN-BM and hBN-AR, a shift from 768 cm ⁻¹ to 773 cm ⁻¹ is observed for
the B-N bending vibration [34]. This shift along with the increase of the intensity of the B-N-
B out-of-plane bending vibration relative to the peak of B-N in-plane transverse optical mode
[9] for hBN-BM can be attributed to the exfoliation and thinning of the hBN nanoplatelets
during ball milling. The spectra of hBN-BM-U and hBN-BM-UsFC are similar to that of hBN-
U and hBN-U _{SFC} indicating successful exfoliation and functionalization, especially for the
ultrasonicated case with surfactants.
The intensity ratio of the peaks at ~3393 cm ⁻¹ and ~1340 cm ⁻¹ can be used to evaluate the
degree of functionalization with hydroxyl groups for hBN-AR and hBN-BM, as shown in
Tables 1 and 2, respectively. The increase in the I_{OH}/I_{B-N} stretching ratio for hBN-BM compared
to hBN-AR confirms the improved functionalization of hBN with hydroxyl groups during ball
milling [32]. Similarly, hBN-U and hBN-BM-U have slightly higher I_{OH}/I_{B-N} stretching ratios,
milling [32]. Similarly, hBN-U and hBN-BM-U have slightly higher I_{OH}/I_{B-N} stretching ratios,
milling [32]. Similarly, hBN-U and hBN-BM-U have slightly higher I_{OH}/I_{B-N} stretching ratios, which can be attributed to ultrasonication fracturing the hBN nanoplatelets, resulting in
milling [32]. Similarly, hBN-U and hBN-BM-U have slightly higher I_{OH}/I_{B-N} stretching ratios, which can be attributed to ultrasonication fracturing the hBN nanoplatelets, resulting in hydroxyl groups attaching to the edges [35]. The I_{OH}/I_{B-N} stretching values further revealed a

Table 1. FTIR bands of hBN-AR, hBN-U, and hBN-U_{SFC} in addition to intensity peak ratios that allow quantification of the degree of functionalization with hydroxyl groups.

		hBN-AR	hBN-U	hBN-U _{SFC}
OII	Wavenumber (cm ⁻¹)	3393.2	3393.7	3393.2
ОН	I _{OH} (%)	89.13	85.5	84.6
B-N stretching	Wavenumber (cm ⁻¹)	1340.3	1340.3	1360.1
D-IN stretching	IB-N stretching (%)	41.05	19.4	12.4
B-N bending	Wavenumber (cm ⁻¹)	768.5	768.5	752.6
D-IN Deliding	I _{B-N} bending (%)	27.6	7.9	13.6
	nsity Ratio I _{B-N stretching}	2.17	4.4	7.3

Table 2. FTIR bands of hBN-BM, hBN-BM-U, and hBN-BM-U_{SFC} in addition to intensity peak ratios that allow quantification of the degree of functionalization with hydroxyl groups.

		hBN-BM	hBN-BM-U	hBN-BM-Usec
OH	Wavenumber (cm ⁻¹)	3393.7	3393.7	3394.7
ОН	I _{OH} (%)	89.77	90.95	84.09
B-N stretching	Wavenumber (cm ⁻¹)	1339.8	1361.04	1366.82
	IB-N stretching (%)	36.39	14.24	11.31
B-N bending	Wavenumber (cm ⁻¹)	772.36	772.36	776.7
D-IN Deliding	I _{B-N bending} (%)	16.7	32.30	5.86
	nsity Ratio I _{B-N} stretching	2.46	6.4	14.8

Raman spectroscopy provides further insight into the characteristics of the hBN nanoplatelets. A typical hBN Raman spectrum, shown in Figure 4, contains a single vibrational peak denoted as E_{2g} at 1366 cm⁻¹ [34]. This peak represents the high-frequency inter-layer Raman active E_{2g} mode of hBN. The variations in the G-band peak width were used to estimate the number of layers of the hBN samples. In particular, the full-width at half-maximum (FWHM_{G-band}) of the hBN G-band extracted from Lorentzian fits allows the number of layers (N) to be calculated using Eq. (5) [32].

$$N = \frac{17.2}{(FWHM_{G-band} - 8.5)} - 1 \tag{2}$$

Upon functionalization, the Raman peak red shifts and full-width at half-maximum increases, indicating the reduced inter-layer interaction of exfoliated products [31]. These results confirm that the ball milling of hBN-AR to produce hBN-BM resulted in improved exfoliation of the hBN nanoplatelets. The results shown in Table 3 indicate the estimated number of layers using Raman analysis in addition to the calculated number of layers from AFM statistical analysis, showing strong agreement between the two methods.

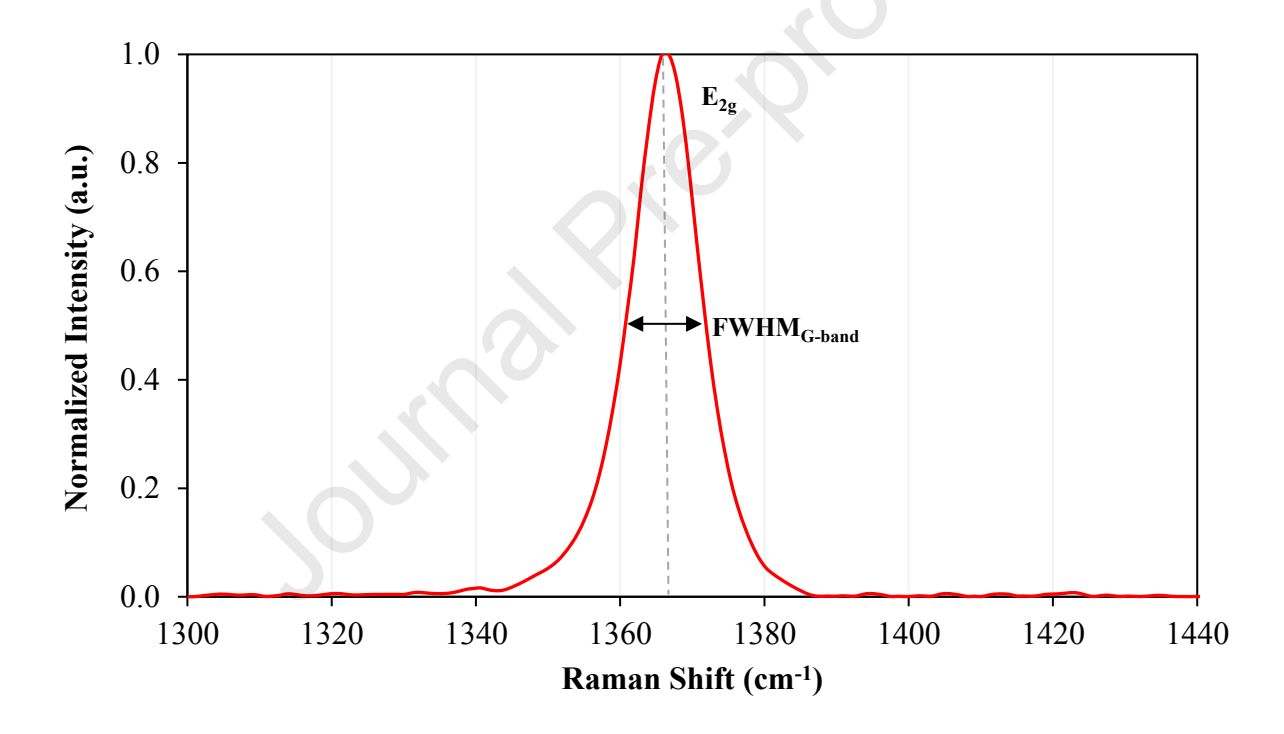


Figure 4. Typical hBN Raman spectrum.

Table 3. Estimated number of hBN layers using AFM measurements and Raman spectroscopy analysis.

	AFM		Raman	
	Number of layers	Raman Shift _{G-band} (cm ⁻¹)	FWHM _{G-band} (cm ⁻¹)	Theoretical number of layers
hBN-AR	12-16	1366.74	10.06	10
hBN-BM	6-9	1363.83	11.21	5
hBN-U	7-11	1364.79	10.81	6
hBN-Usec	5-8	1362.87	11.35	5
hBN-BM-U	5-8	1361.91	11.61	4
hBN-BM-U _{SFC}	3-4	1359.97	12.61	3

Zeta potential values were recorded throughout the ultrasonication procedure to identify the optimum amount of applied ultrasonication energy for achieving stable suspensions. Figures 5a and 5b present the absolute zeta potential values at ultrasonication energies up to 2000 kJ/L. Prior to sonication, suspensions exhibit values lower than 30 mV, which indicate unstable hydrophobic suspensions [6]. The zeta potential of the hBN-AR and hBN-BM suspensions increases with the application of ultrasonication energy up to 1800 kJ/L, indicating improved suspension stability. The highest increase in zeta potential values occurs at 1800 kJ/L. For higher ultrasonication energies, the absolute zeta potential values exhibit a plateau, indicating that the stability of the suspensions is no longer improved. The stability of the hBN-BM-U and hBN-BM-Usrc suspensions was found to be higher than that of hBN-U and hBN-Usrc at all energies. This observation can be attributed to the hydroxyl groups grafted onto hBN-BM increasing the hydrophilicity of the hBN nanosheets, resulting in increased dispersibility and stability in aqueous suspensions. In addition, the use of surfactants during ultrasonication results in a higher zeta potential, indicating a significantly improved colloidal stability, mainly due to electrostatic and steric effects introduced by the surfactant [36].

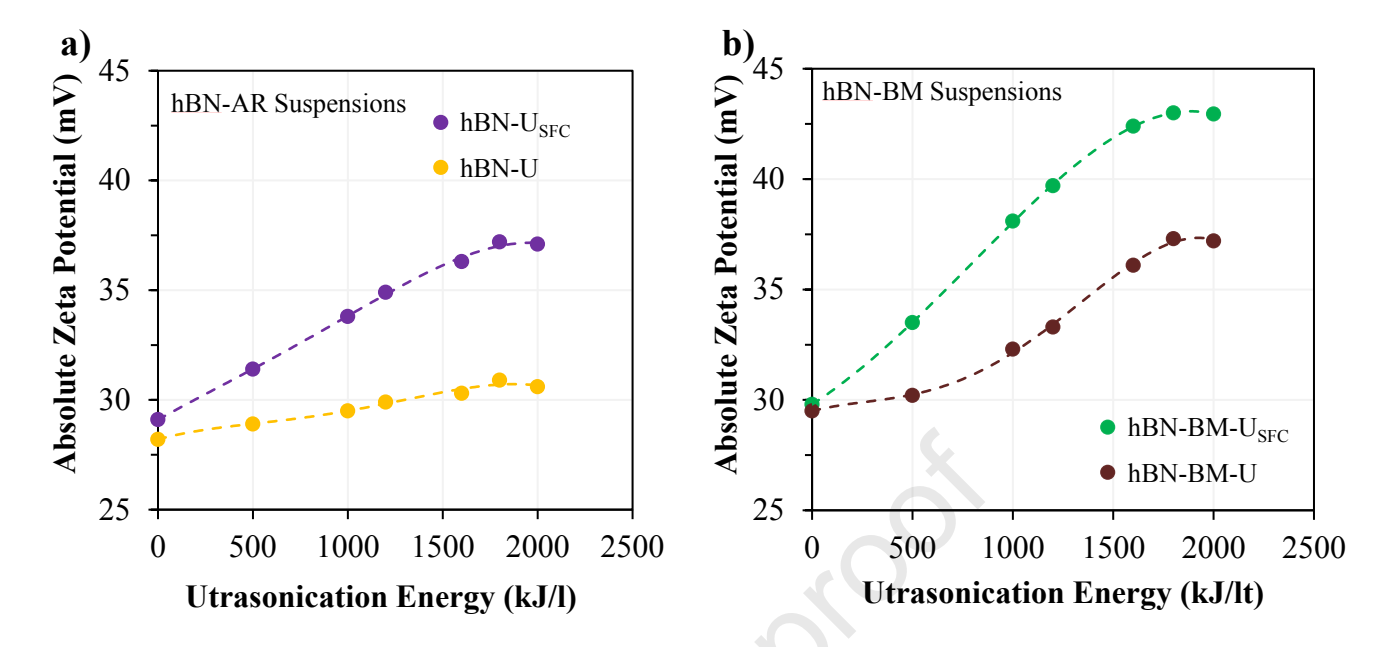
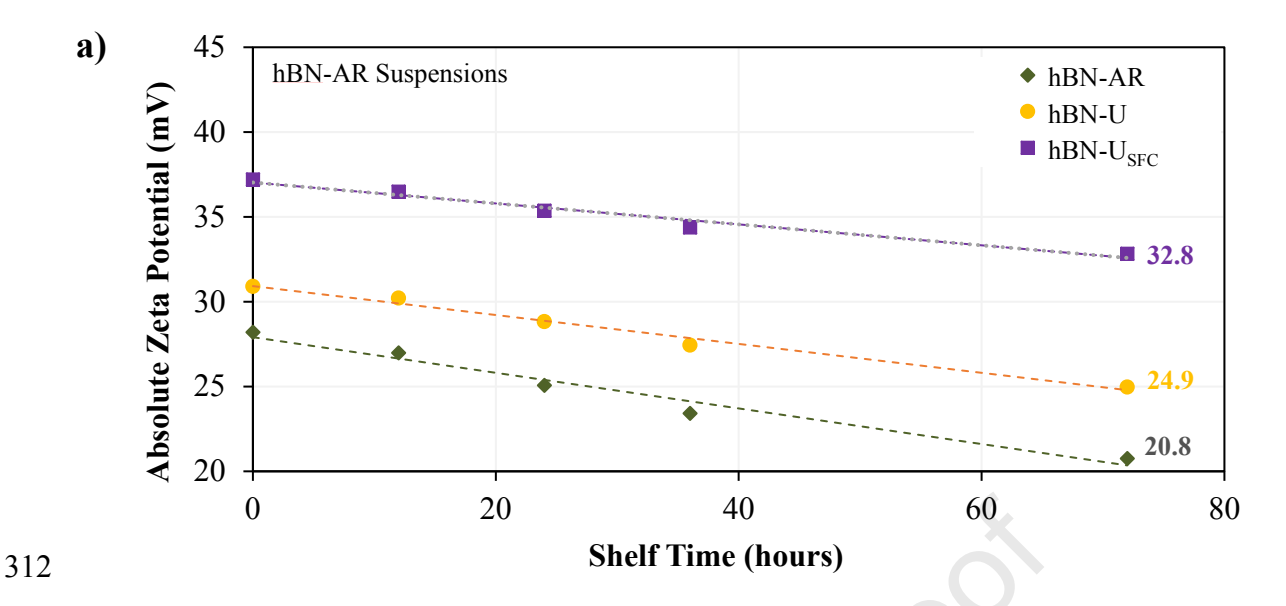


Figure 5 Absolute zeta potential of (a) hBN-U and hBN- U_{SFC} and (b) hBN-BM-U and hBN-BM-U_{SFC} suspensions as a function of ultrasonication energy.

The values of absolute zeta potential of the hBN-AR and hBN-BM suspensions were systematically measured over a period of 3 days with the results being presented in Figures 6a and 6b. A decrease in zeta potential values with increasing shelf time ranging from 12 to 26% was observed for the hBN-AR suspensions, whereas the hBN-BM suspensions exhibit decreases in the range of 5-15%. Specifically, the stability of the hBN-BM-UsFC suspensions was found to be only 15% lower compared to that shortly after the completion of the ultrasonication procedure and remained higher than that of hBN-UsFC due to the hydroxyl groups grafted on hBN-BM.



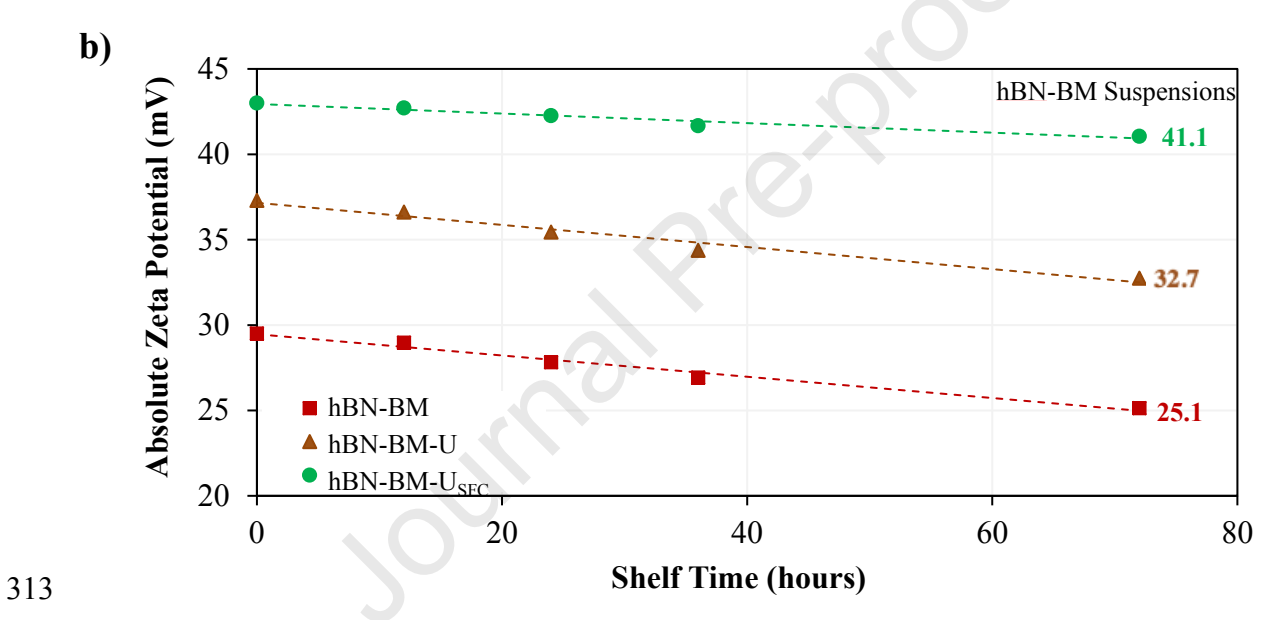


Figure 6. Absolute zeta potential measurements as a function of shelf time for the (a) hBN-AR and (b) hBN-BM suspensions.

321 3.2 Effects of hBN on Cement Hydration

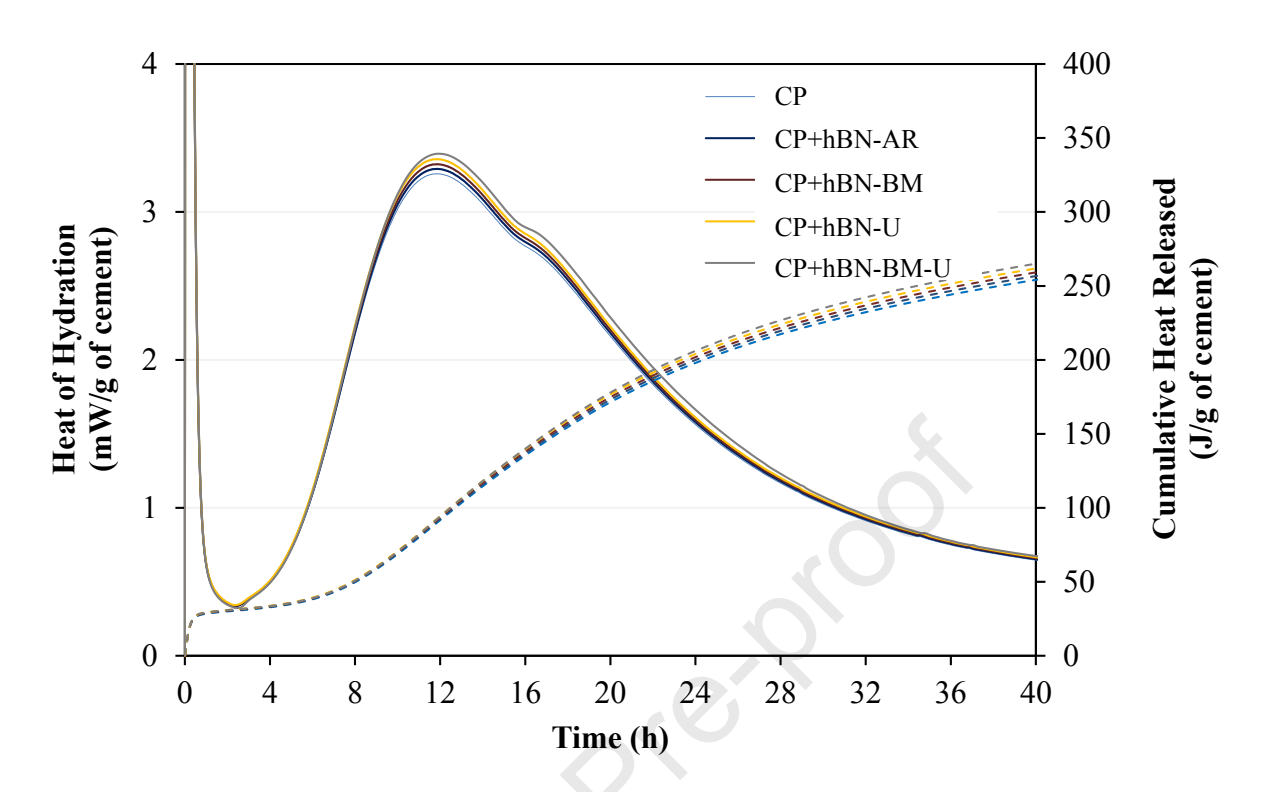


Figure 7. Heat of hydration (solid lines) and cumulative heat released (dashed lines) curves of plain and hBN-AR, hBN-BM, hBN-U and hBN-BM-U reinforced cement paste mixes

The isothermal calorimetry results in Figure 7 present the effect of the addition of as-received (AR), ball-milled (BM), and ultrasonicated (U) hBN on cement hydration. The heat of hydration – time curves show that compared to plain OPC paste the addition of 0.18 vol% hBN marginally increases the heat of hydration, probably due to the high intrinsic thermal conductivity of the boron nanoplatelets [1]. Comparing the cumulative heat released during hydration also confirmed that cement paste mixes reinforced with the as-received, ball-milled and ultrasonicated hBN exhibit almost the same hydration behavior to that of plain cement. Zhang et al. [37] have also observed no changes in the degree of cement hydration with the addition of boron nitride nanoplatelets, through X-ray diffraction (XRD) analysis.

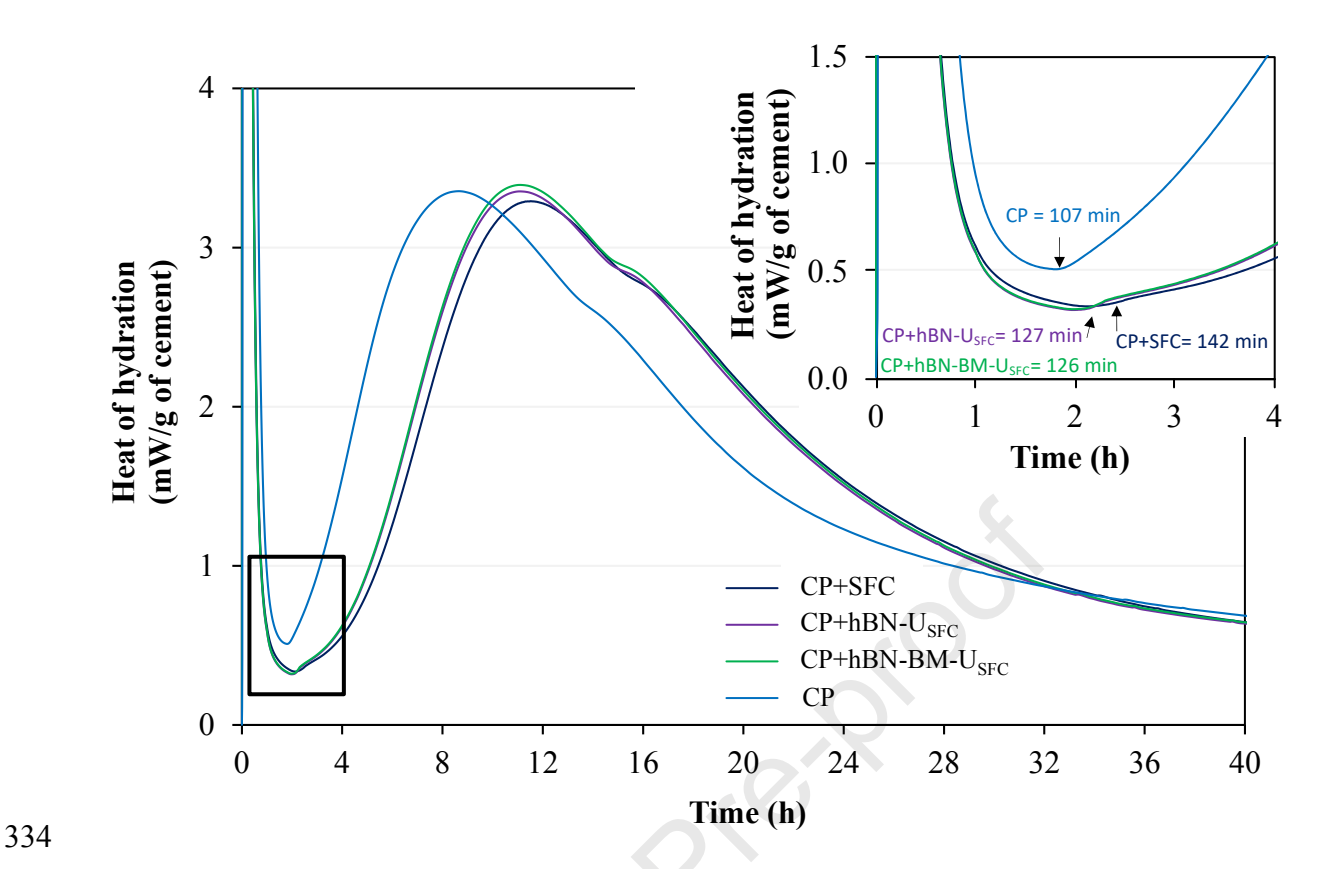


Figure 8. Heat of hydration curves of plain and hBN-U_{SFC}, and hBN-BM-U_{SFC} reinforced cement paste mixes with the use of surfactant (SFC)

The isothermal calorimetry results of plain and hBN cement pastes with the use of surfactant (SFC) are presented in Figure 8. It has long been recognized that the use of polycarboxylate SFC may retard the hydration process of cement [38]. As depicted from the heat of hydration – time curves in Figure 8, the CP + SFC mix exhibits an induction period (142 min) extended by \approx 25 min compared to the CP without the SFC addition (107 min). The addition of exfoliated boron nanoplatelets (hBN-UsFC and hBN-BM-UsFC) led to a less extended induction period of of CP+hBN-UsFC and CP+hBN+BM+UsFC, 127 min and 126 min, respectively. Assuming that a good amount of SFC is adsorbed on the boron nanoplatelets surface, less amount of the surfactant is available in the cementitious matrix to interact with cement, when compared with the plain cement paste mix that contains the same amount of SFC [19, 39].

3.3 Effects of hBN Functionalization and Exfoliation on the Mechanical Properties of Nanoreinforced Mortars

Since effective exfoliation and functionalization allows better interfacial bonding between nanomaterials and cementitious matrices, the hBN suspensions were used to develop cementitious nanocomposites and study the impact of hBN exfoliation and functionalization on the strength and stiffness of hBN-cement nanocomposites. Figure 9 presents the rate of flexural strength development of the 28d mortar nanocomposites reinforced with as-received (AR), ball-milled (BM), and ultrasonicated (U) hBN at 0.18 % volume fraction. All hBN-reinforced mortars exhibit higher flexural strength than the plain mortar at all ages. Mortars reinforced with hBN-AR or hBN-BM show relatively minor increases in the 28d flexural strength of about 12%. hBN-U and hBN-BM-U reinforced mortars exhibited a 17.6% and 24.2% increase in flexural strength, respectively. Addition of hBN-BM-U_{SFC} yields the highest ability to carry flexural loads with an increase of 51.3% in flexural strength compared to plain mortar specimens.

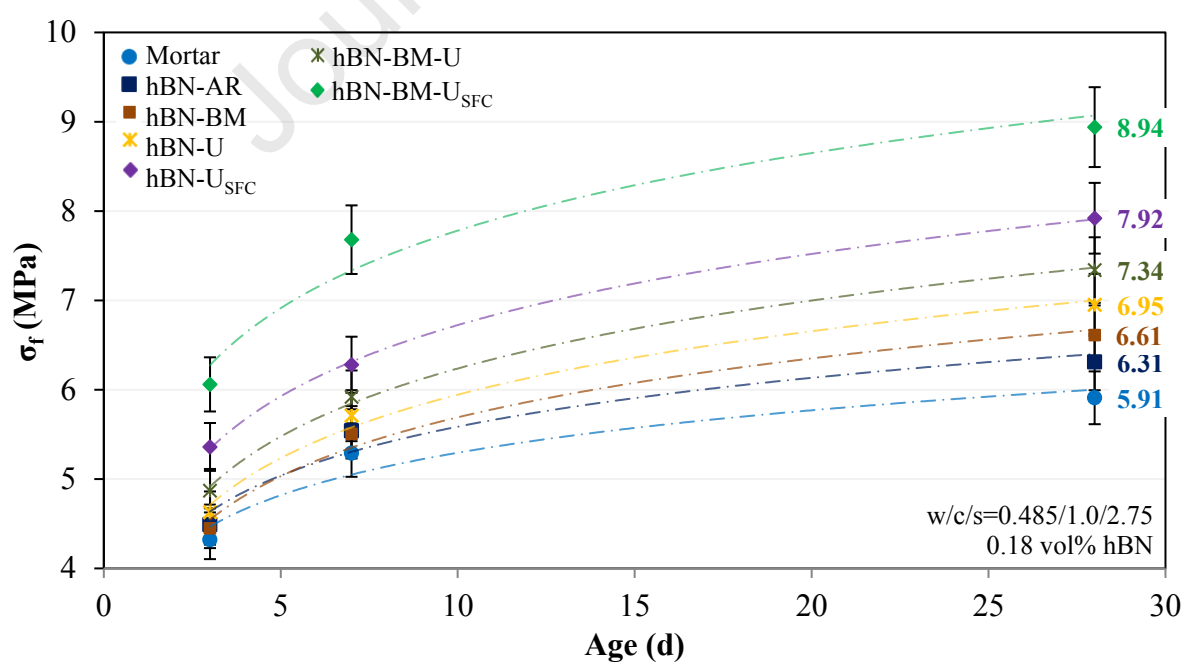


Figure 9. Flexural strength, σ_f , of mortars reinforced with 0.18 vol% hBN at the age of 3, 7, and 28 days.

The enhanced load bearing capacity of hBN-BM-U_{SFC} reinforced mortars can be attributed to the increased surface area and homogeneous distribution of thin, functionalized hBN nanoplatelets, which can induce strong interactions with the cementitious products, resulting in crack inhibition of the mortar matrix. hBN nanoplatelets with hydroxyl and carboxyl groups grafted on their surface exhibit similar behavior to that of carbon-based functionalized nanomaterials [40]. The Ca²⁺ ions present in the calcium silicate hydrates (C-S-H) undergo covalent reactions with the functional groups attached to the surface of hBN [41]. Due to this interaction, hydration products are formed between interlocking hBN sheets, establishing a strong bond at the interface between the hBN and C-S-H that promotes efficient load transfer. Compared to the mortars reinforced with hBN after ball milling and ultrasonication (hBN-BM-U_{SFC}), the composites with sonicated hBN-AR (hBN-U and hBN-U_{SFC}) exhibit 13-28% lower flexural strength. As shown in Figure 1 and Table 3, boron nanoplatelets after ultrasonication exhibit a thickness of 8 nm while hBN after ball milling and ultrasonication (hBN-BM-U) show a thickness of 5 nm, which is consistent with the mechanical testing results. The effective exfoliation process through ball milling and ultrasonication significantly increases the surface area of the functionalized hBN network available for reactions with Ca²⁺ ions, thus enhancing more effectively the interfacial bond strength between the hBN and the cementitious matrix [41-42]. The intrinsic strength of the hBN depends on their thickness, where the 5 nm thick hBN exhibit strength values of 250 MPa, 25% higher than the strength (200 MPa) of the 8 nm thick hBN [43-44]. The enhanced interfacial bonding between the thinner hBN and cementitious matrix may also lead to a more effective load transfer mechanism increasing the nanocomposite's flexural strength.

385

363

364

365

366

367

368

369

370

371

372

373

374

375

376

377

378

379

380

381

382

383

384

Table 4. Tensile and Compressive Young's modulus, E, of mortars reinforced with 0.18 vol% hBN at the age of 3, 7, and 28 days.

	Age (d)	Young's modulus, E (GPa) 3 point bending 40×40×160 mm ³	Young's modulus, E (GPa) Compression 40×40×80 mm ³
	3	9.23 ± 0.24	9.46 ± 0.44
Mortar	7	11.15 ± 0.81	11.57 ± 0.58
	28	14.30 ± 1.28	14.10 ± 0.25
	3	10.23 ± 0.75	11.00 ± 0.25
hBN-AR	7	12.42 ± 0.98	12.12 ± 0.30
	28	17.22 ± 1.16	17.73 ± 1.06
	3	10.43 ± 0.76	11.40 ± 0.41
hBN-BM	7	12.98 ± 1.00	12.53 ± 0.60
	28	17.51 ± 1.11	17.55 ± 0.53
	3	9.45 ± 0.60	9.22 ± 0.42
hBN-U	7	11.61 ± 0.94	11.87 ± 0.34
	28	14.64 ± 1.30	14.29 ± 0.34
	3	12.40 ± 1.00	12.90 ± 0.44
hBN-Usfc	7	15.38 ± 0.81	15.76 ± 0.20
	28	21.42 ± 1.33	21.37 ± 0.32
	3	10.86 ± 0.89	11.23 ± 0.46
hBN-BM-U	7	13.95 ± 0.99	13.41 ± 0.60
	28	19.10 ± 0.93	19.47 ± 0.58
	3	13.25 ± 0.90	13.05 ± 0.80
hBN-BM-Usec	7	16.57 ± 1.14	16.84 ± 0.57
	28	22.31 ± 0.57	22.98 ± 0.42

The Young's modulus results for plain mortar and 0.18 vol% hBN reinforced mortars are presented in Table 4. Similar to the flexural strength results, the Young's modulus increases with the addition of hBN to the cementitious matrix. Compared to plain mortars, relatively minor increases in the Young's modulus were observed for the hBN-AR and hBN-BM mortars. The 28-day hBN-U and hBN-BM-U nanoreinforced mortars exhibit a 27.3% and 33.6% increase in Young's modulus, respectively. Results from the Young's modulus using hBN-BM-Usec show the significance of the addition of the surfactant towards modulus enhancement, as

an increase of 56% was observed. This is attributed to the attachment of carboxyl and hydroxyl groups from the surfactant used for the exfoliation process onto the hBN surface [40] resulting in increased covalent reactions with the Ca^{2+} ions from C-S-H that promote a much higher load bearing capacity of the hBN-BM-U_{SFC} cementitious composites at the elastic stage [41, 44]. Therefore, the hBN-BM-U_{SFC} nanocomposites exhibit a \approx 1.6x higher Young's modulus than the mortars reinforced with the hBN-BM-U, exfoliated without the use of surfactant.

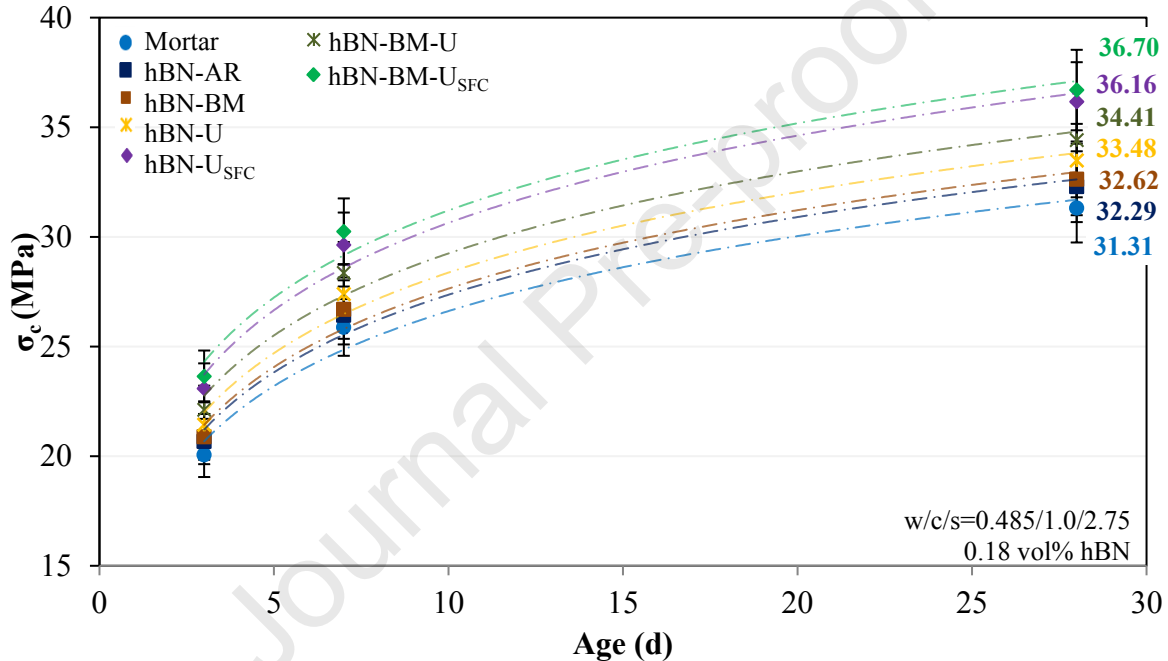


Figure 10. Compressive strength, σ_c , of mortars reinforced with 0.18 vol% hBN at the age of 3, 7, and 28 days.

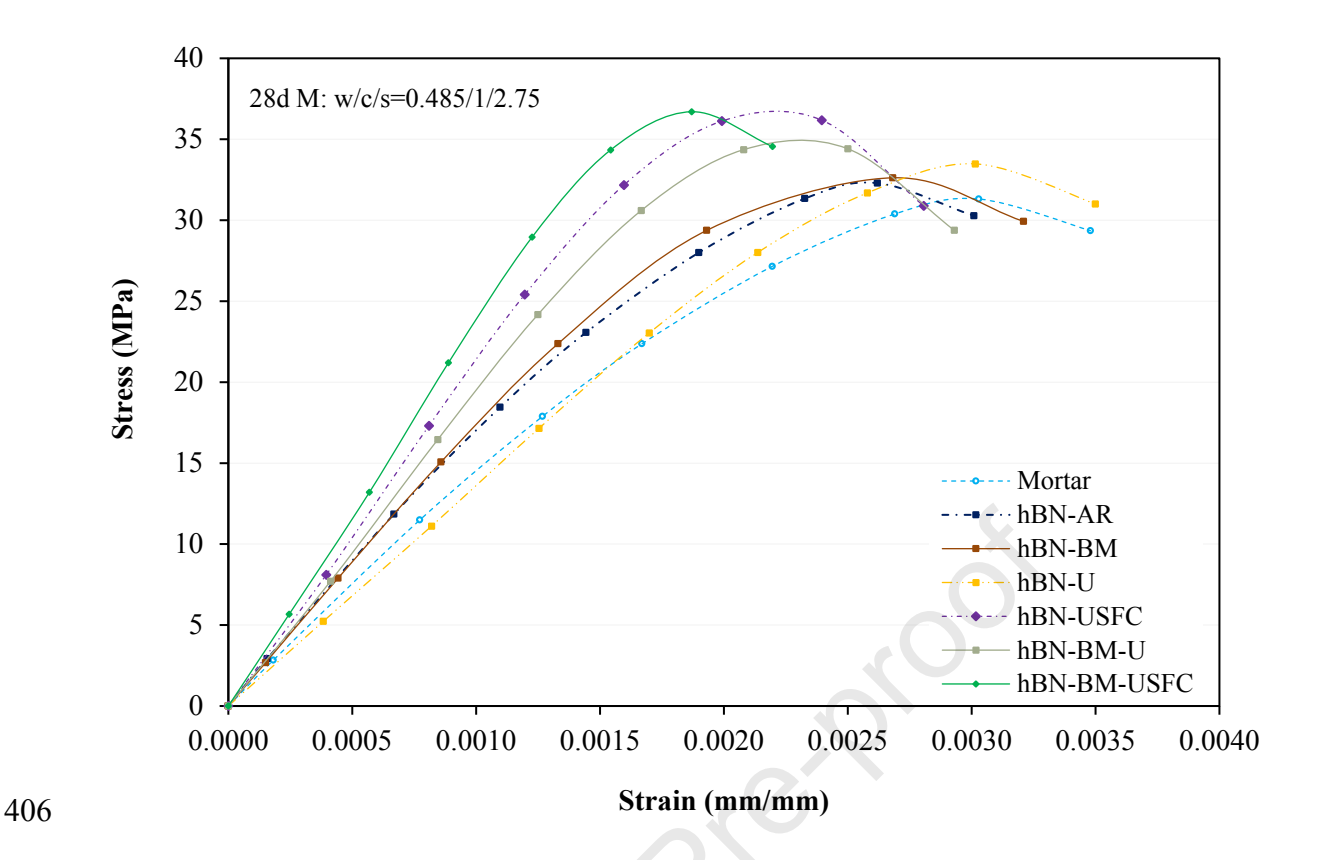


Figure 11. Compressive stress-strain curves of 28 d plain mortar and mortars reinforced with 0.18 vol% hBN

The compressive strength, σ_c , of the plain mortar and mortars reinforced with 0.18 vol% hBN is depicted in Figure 10. A modest improvement in compressive strength was observed with the 28-day hBN mortars exhibiting slight increases in compressive strength ranging from 3% to 17%. The compressive stress-strain curves of 28 d plain and 0.18 vol% hBN reinforced mortars are presented in Figure 11. The compressive modulus values of all mortars are calculated by the initial compliance of each curve according to the ASTM C 469 and presented in Table 4. Despite the modest increase of the compressive strength, the use of effectively exfoliated and functionalized hBN significantly increases the stiffness. It should be noted here that the compressive modulus values (Table 4) perfectly agree with the values determined from the three-point bending tests.

Such enhancements in the flexural strength and Young's modulus indicate strong interactions between thin, functionalized hBN nanoplatelets and cementitious products that may increase the demand of strain energy for crack propagation. The amount of strain energy necessary for the crack initiation and propagation in a cementitious material is represented by the fracture energy, G_f [30]. The fracture energy can be calculated from the load to crack mouth opening displacement (CMOD) response of notched specimens subjected to Linear Elastic Fracture Mechanics tests (LEFM) following the RILEM 50-FMC equation [30]:

$$G_f = \frac{W_0 + mgCMOD_0}{4} \tag{3}$$

Where, m is the self weight of the specimen, g gravitational acceleration constant (9.81 m/s²), A the reduced cross sectional area in the notch region, CMOD₀ the CMOD value at failure and W_0 the area under the load – CMOD curve (work). Load – CMOD curves of 28-day plain mortar and mortar reinforced with the ball milled hBN after ultrasonication with the use of surfactant (hBN-BM-U_{SFC}) are shown in Figure 12.

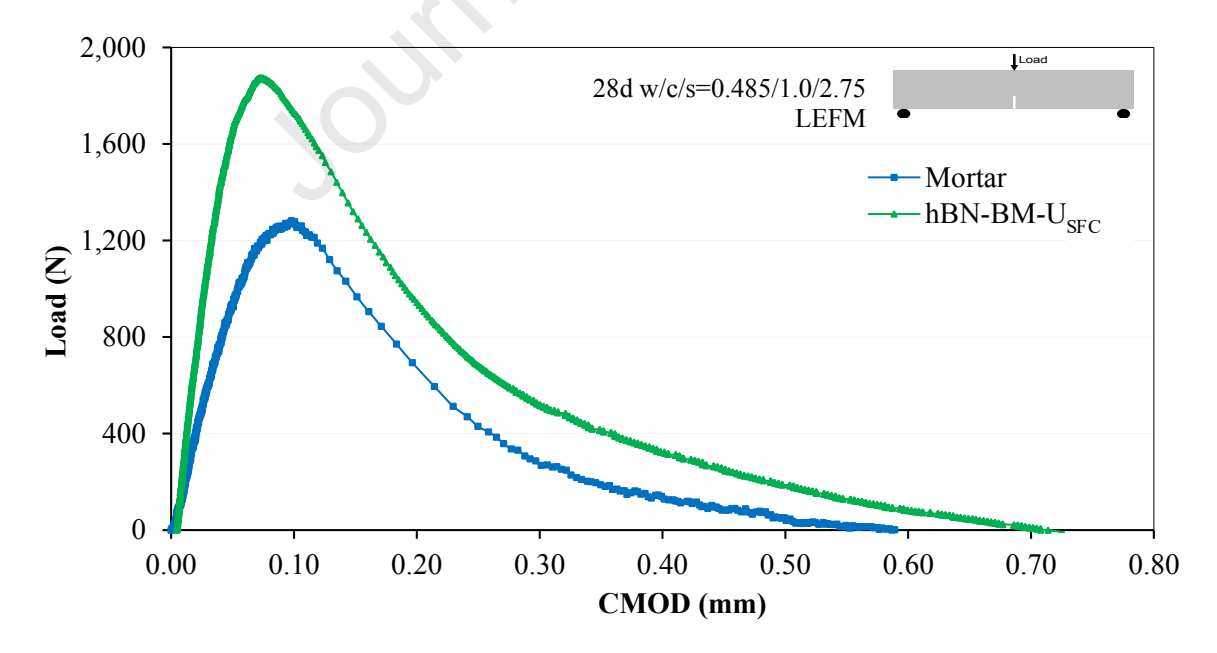


Figure 12. Load - CMOD curves of 28 d plain mortar and mortar reinforced with 0.18 vol% hBN-BM-U_{SFC}

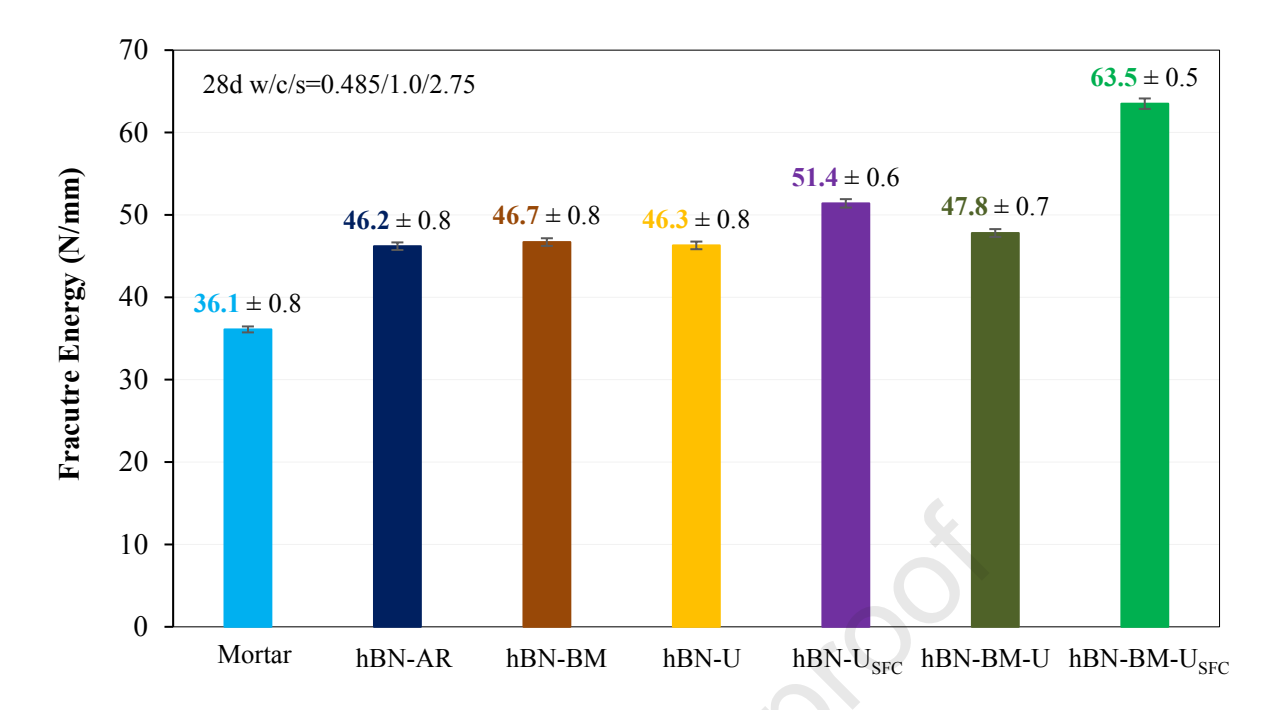


Figure 13. Fracture Energy, G_f, of 28-day mortars reinforced with 0.18 vol% hBN.

Load – CMOD curves of both the plain and hBN-BM-U_{SFC} reinforced mortars in Figure 12 exhibit the same pattern, consisting of a linear elastic stage before crack initiation, nonlinear stage of stable crack propagation, preceding unstable failure and unstable extension stage after the peak load. It is observed however, that the total area under the load – CMOD curve (work, W_0) of the hBN-BM-U_{SFC} reinforced mortar is much higher compared to the plain mortar, therefore the fracture energy is expected to be increased. The fracture energy results of the 28-day plain and hBN reinforced mortars calculated from Eq. 3 are presented in Figure 13. The nanocomposites reinforced with hBN-BM-U_{SFC} yielded the highest increase in fracture energy of 76% over the plain mortar. Relatively moderate increases in the fracture energy ranging from 27 – 40% were observed for the 28-day hBN-AR, hBN-BM, hBN-U, hBN-U_{SFC} and hBN-BM-U mortars. This is in accordance with the trend already observed for the flexural strength (Figure 9) and Young's modulus (Table 4). Generally, the improvement of the fracture energy indicates that a significantly higher amount of energy is required for crack initiation and propagation in a cementitious system reinforced with nanomaterials.

Table 5. Summary of Flexural strength, Compressive strength, Young's modulus and fracture energy results of 28-day plain and hBN reinforced mortars

	Flexural strength (MPa)	Compressive strength (MPa)	Young's modulus (GPa)	Fracture Energy (N/mm)
Mortar	5.91 ± 0.11	31.31 ± 1.27	14.30 ± 1.28	36.1 ± 0.81
hBN-AR	6.31 ± 0.11	32.29 ± 1.26	17.22 ± 1.16	46.2 ± 0.80
hBN-BM	6.66 ± 0.11	32.62 ± 1.26	17.51 ± 1.11	46.7 ± 0.81
hBN-U	6.95 ± 0.10	33.48 ± 1.08	14.64 ± 1.30	46.3 ± 0.81
hBN-Usfc	7.92 ± 0.08	36.16 ± 0.93	21.42 ± 1.33	51.4 ± 0.62
hBN-BM-U	7.34 ± 0.08	34.41 ± 0.97	19.10 ± 0.93	47.8 ± 0.71
hBN-BM-Usec	8.94 ± 0.07	36.70 ± 0.91	22.31 ± 0.57	63.5 ± 0.52

Overall, it is clear that increased surface functionalization and exfoliation of hBN nanoplatelets within the cementitious matrix holds great potential for improving the mechanical properties of cementitious nanocomposites [41-44]. The 28-day cementitious composites reinforced with the thin, functionalized hBN after ball milling and ultrasonication (hBN-BM-U_{SFC}) outperformed all other mixes, exhibiting the highest increases in flexural strength (50%), compressive strength (17%), Young's modulus (56%) and fracture energy (76%) over the plain mortar as shown in Table 5.

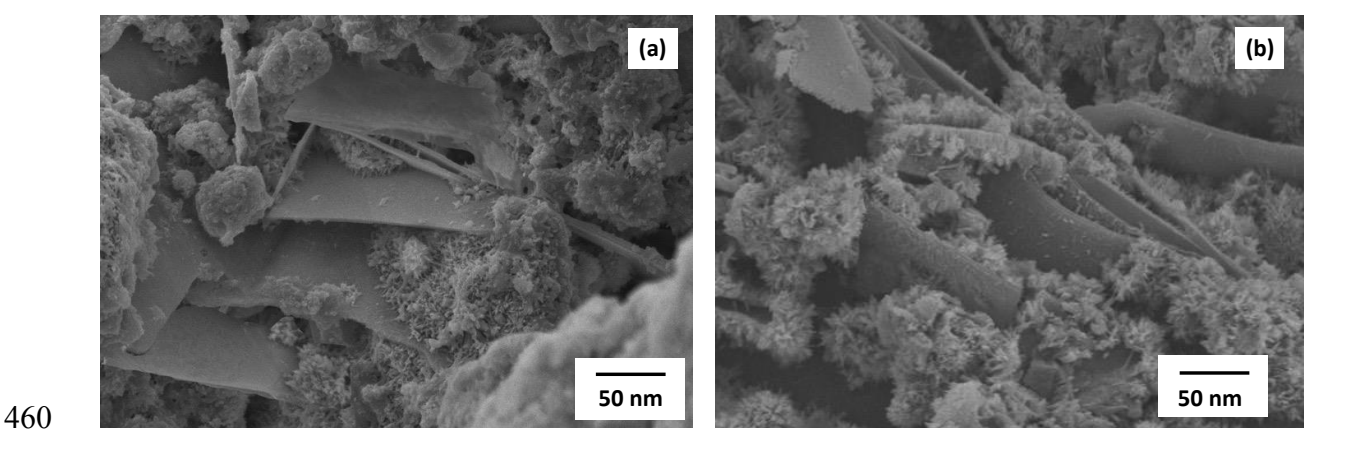


Figure 14 (a) and (b). SEM images of the fracture surface of cement nanocomposites reinforced with hBN-BM- U_{SFC}

Figures 14 a and b show SEM images of fracture surfaces of the samples reinforced with hBN-BM-UsFC at a scale of 50 nm. Thin hBN after ball milling and ultrasonication (hBN-BM-UsFC) with a typical plate-like structure [45] are observed. The plate-like structure of individual hBN layers after the ball milling and ultrasonication process was also identified in AFM images in Figure 1. It is revealed from the SEM images in Figures. 14 a and b that the surface of hBN is covered with C-S-H. The observations suggest that not only an effective exfoliation of hBN into the cementitious matrix was achieved; also the hBN layers themselves are intercalated within the matrix, which enhances the interfacial bonding and enables an effective load transfer between the matrix and hBN, resulting in the improvement of the overall mechanical properties of the nanocomposite.

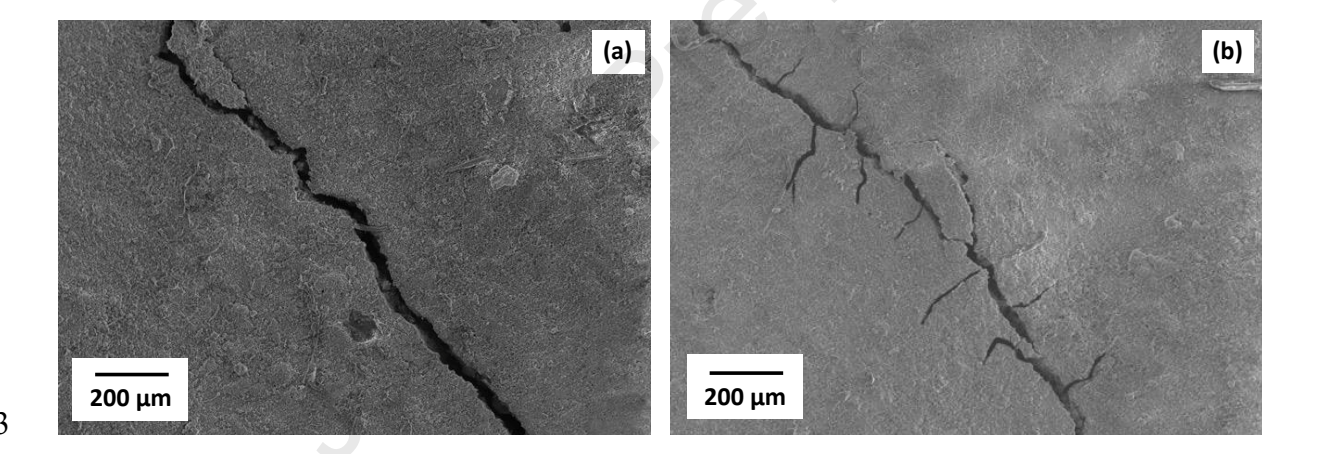


Figure 15. Typical SEM images showing the crack pathways on the fracture surfaces of (a) hBN-BM-U mortar and (b) hBN-BM-U_{SFC} mortar

The plate-like structure of the thin hBN after ball milling and ultrasonication with the use of surfactant (hBN-BM-U_{SFC}) may also contribute to the development of more articulated crack paths resulting in a more effective stress redistribution into the matrix [46]. SEM images of the micro-cracks on the fracture surface of hBN-BM-U and hBN-BM-U_{SFC} reinforced mortars at a 200 µm resolution are presented in Figure 15 a and b, respectively. It is observed that the pathway of the micro-crack on the fracture surface of hBN-BM-U_{SFC} mortars appears more

tortuous with multiple crack branching, while the micro-crack on the surface of hBN-BM-U mortars follows a more linear pathway. The formation of multiple and tortuous microcracks in cementitious matrices is indicative of a controlled crack growth process that allows the nanocomposite to greatly improve its strain energy demands for crack initiation and propagation greatly improving the overall strength, stiffness and strain energy capacity of the nanocomposites.

4. Conclusions

Well-exfoliated and functionalized hBN nanoplatelets were successfully produced from bulk hBN using a combination of ball-milling and ultrasonication. The hBN suspensions were characterized by a series of spectroscopic and microscopic experiments to assess the stability, exfoliation quality, and functionalization degree. FTIR and zeta potential data revealed that functionalization of hBN through ball milling and ultrasonication, particularly with the use of a cementitious materials surfactant, resulted in the presence of hydroxyl and carboxyl groups, which in turn led to increased hydrophilicity of hBN and steric or electrostatic repulsions that enhance the stability of the aqueous suspensions. The degree of exfoliation was also confirmed by atomic force microscopy. AFM imaging was used to characterize the thickness of the hBN nanoplatelets, confirming reduced thickness after exfoliation and functionalization. The theoretical number of hBN layers was determined through Raman spectroscopy. The results are in perfect agreement with the number of layers identified through AFM analysis.

High-performance hBN cementitious nanocomposites are ideally suited to attaining improved mechanical properties as a result of their high surface area and -OH and -COOH grafted onto the hBN surface. The attached functional groups on the hBN surface undergo covalent reactions with the Ca²⁺ ions in C-S-H. Due to this interaction, a strong bond at the interface between the hBN and C-S-H is established that improves the load transfer efficiency from the

506	cementitious matrix to the hBN nanoplatelets. The enhanced load bearing capacity of the hBN
507	reinforced mortars is demonstrated by improvements in flexural strength, 50%, compressive
508	strength, 17%, Young's modulus, 56%, and fracture energy, 76%.
509	The exceptional properties of high-performance hBN cementitious nanocomposites render
510	them an ideal candidate for multifunctional applications, due to the unique intrinsic properties,
511	the very small thickness, and grafted hydroxyl and carboxyl groups functional groups on the
512	hBN surface that enhance the interfacial interactions between the hBN nanoplatelets and the
513	matrix. The authors of this work will further evaluate the properties of cementitious
514	nanocomposites with highly functionalized tri-layered hBN in future work, paving new
515	pathways toward the use of hBN cementitious nanocomposites in energy related applications.
516	Acknowledgments
517	The authors acknowledge support from the National Science Foundation Partnerships for
518	Research and Education in Materials (Award Number NSF DMR-2122128) and the
519	
31)	Northwestern University Materials Research Science and Engineering Center (Award Number
520	Northwestern University Materials Research Science and Engineering Center (Award Number NSF DMR-1720139). Master Builders Solutions Admixtures US, LLC is kindly acknowledged
520	NSF DMR-1720139). Master Builders Solutions Admixtures US, LLC is kindly acknowledged
520 521	NSF DMR-1720139). Master Builders Solutions Admixtures US, LLC is kindly acknowledged for providing the chemical admixtures. C.M.T. gratefully acknowledges the support of the
520521522	NSF DMR-1720139). Master Builders Solutions Admixtures US, LLC is kindly acknowledged for providing the chemical admixtures. C.M.T. gratefully acknowledges the support of the
520521522523	NSF DMR-1720139). Master Builders Solutions Admixtures US, LLC is kindly acknowledged for providing the chemical admixtures. C.M.T. gratefully acknowledges the support of the

References

- 528 [1] Jo, I., Pettes, M.T., Kim, J., Watanabe, K., Taniguchi, T., Yao, Z. and Shi, L., 2013. Thermal
- 529 conductivity and phonon transport in suspended few-layer hexagonal boron nitride. Nano
- 530 letters, 13 (2), pp. 550-554.
- 531 [2] Golberg, D., Bando, Y., Huang, Y., Terao, T., Mitome, M., Tang, C. and Zhi, C., 2010.
- Boron nitride nanotubes and nanosheets. ACS nano, 4(6), pp.2979-2993.
- 533 [3] Falin, A., Cai, Q., Santos, E.J., Scullion, D., Qian, D., Zhang, R., Yang, Z., Huang, S.,
- Watanabe, K., Taniguchi, T. and Barnett, M.R., 2017. Mechanical properties of atomically thin
- boron nitride and the role of interlayer interactions. Nature communications, 8 (1), pp. 1-9.
- [4] Secor, E.B. and Hersam, M.C., 2015. Emerging carbon and post-carbon nanomaterial inks
- for printed electronics. The journal of physical chemistry letters, 6 (4), pp. 620-626.
- [5] Kang, J., Sangwan, V.K., Wood, J.D. and Hersam, M.C., 2017. Solution-based processing
- of monodisperse two-dimensional nanomaterials. Accounts of chemical research, 50 (4), pp.
- 540 943-951.
- 541 [6] Yao, Y., Lin, Z., Li, Z., Song, X., Moon, K.S. and Wong, C.P., 2012. Large-scale production
- of two-dimensional nanosheets. Journal of Materials Chemistry, 22 (27), pp. 13494-13499.
- [7] Lee, D., Lee, B., Park, K.H., Ryu, H.J., Jeon, S. and Hong, S.H., 2015. Scalable exfoliation
- process for highly soluble boron nitride nanoplatelets by hydroxide-assisted ball milling. Nano
- 545 letters, 15 (2), pp. 1238-1244.
- 546 [8] Bai, Y., Zhang, J., Wang, Y., Cao, Z., An, L., Zhang, B., Yu, Y., Zhang, J. and Wang, C.,
- 547 2019. Ball milling of hexagonal boron nitride microflakes in ammonia fluoride solution gives

- 548 fluorinated nanosheets that serve as effective water-dispersible lubricant additives. ACS
- 549 Applied Nano Materials, 2 (5), pp. 3187-3195.
- 550 [9] Du, M., Wu, Y. and Hao, X., 2013. A facile chemical exfoliation method to obtain large
- size boron nitride nanosheets. CrystEngComm, 15 (9), pp. 1782-1786.
- 552 [10] Kim, K.K., Hsu, A., Jia, X., Kim, S.M., Shi, Y., Hofmann, M., Nezich, D., Rodriguez-
- Nieva, J.F., Dresselhaus, M., Palacios, T. and Kong, J., 2012. Synthesis of monolayer
- hexagonal boron nitride on Cu foil using chemical vapor deposition. Nano letters, 12 (1), pp.
- 555 161-166.
- 556 [11] Zhi, C., Bando, Y., Tang, C., Kuwahara, H. and Golberg, D., 2009. Large-scale fabrication
- of boron nitride nanosheets and their utilization in polymeric composites with improved
- thermal and mechanical properties. Advanced Materials, 21 (28), pp. 2889-2893.
- 559 [12] Zhou, K.G., Mao, N.N., Wang, H.X., Peng, Y. and Zhang, H.L., 2011. A mixed-solvent
- strategy for efficient exfoliation of inorganic graphene analogues. Angewandte Chemie, 123
- 561 (46), pp. 11031-11034.
- [13] Marsh, K.L., Souliman, M. and Kaner, R.B., 2015. Co-solvent exfoliation and suspension
- of hexagonal boron nitride. Chemical communications, 51 (1), pp. 187-190.
- 564 [14] Zhu, J., Kang, J., Kang, J., Jariwala, D., Wood, J.D., Seo, J.W.T., Chen, K.S., Marks, T.J.
- and Hersam, M.C., 2015. Solution-processed dielectrics based on thickness-sorted two-
- dimensional hexagonal boron nitride nanosheets. Nano letters, 15 (10), pp. 7029-7036.
- 567 [15] Warner, J.H., Rummeli, M.H., Bachmatiuk, A. and Buchner, B., 2010. Atomic resolution
- imaging and topography of boron nitride sheets produced by chemical exfoliation. ACS nano,
- 569 4 (3), pp. 1299-1304.

- 570 [16] Ma, Z.S., Ding, H.L., Liu, Z. and Cheng, Z.L., 2019. Preparation and tribological
- 571 properties of hydrothermally exfoliated ultrathin hexagonal boron nitride nanosheets (BNNSs)
- in mixed NaOH/KOH solution. Journal of Alloys and Compounds, 784, pp. 807-815.
- 573 [17] Kovtyukhova, N.I., Perea-López, N., Terrones, M. and Mallouk, T.E., 2017. Atomically
- 574 thin layers of graphene and hexagonal boron nitride made by solvent exfoliation of their
- 575 phosphoric acid intercalation compounds. ACS nano, 11 (7), pp. 6746-6754.
- 576 [18] de los Reyes, C.A., Hernández, K., Martínez-Jiménez, C., Walz Mitra, K.L., Ginestra, C.,
- 577 Smith McWilliams, A.D., Pasquali, M. and Martí, A.A., 2019. Tunable alkylation of white
- 578 graphene (hexagonal boron nitride) using reductive conditions. The Journal of Physical
- 579 Chemistry C, 123 (32), pp. 19725-19733.
- 580 [19] Wang, W., Chen, S.J., De Souza, F.B., Wu, B. and Duan, W.H., 2018. Exfoliation and
- dispersion of boron nitride nanosheets to enhance ordinary Portland cement paste. Nanoscale,
- 582 10 (3), pp. 1004-1014.
- 583 [20] Hyun, W.J., Thomas, C.M., Chaney, L.E., Mazarin de Moraes, A.C. and Hersam, M.C.,
- 584 2022. Screen-Printable Hexagonal Boron Nitride Ionogel Electrolytes for Mechanically
- Deformable Solid-State Lithium-Ion Batteries. Nano letters, 22 (13), pp. 5372-5378.
- 586 [21] Hyun, W.J., Thomas, C.M., Luu, N.S. and Hersam, M.C., 2021. Layered
- 587 heterostructure ionogel electrolytes for high-performance solid-state lithium-ion batteries.
- 588 Advanced Materials, 33 (13), p. 2007864.
- 589 [22] Rafiee, M.A., Narayanan, T.N., Hashim, D.P., Sakhavand, N., Shahsavari, R., Vajtai,
- 590 R. and Ajayan, P.M., 2013. Hexagonal boron nitride and graphite oxide reinforced
- multifunctional porous cement composites. Advanced Functional Materials, 23 (45), pp. 5624-
- 592 5630.

- 593 [23] Konsta-Gdoutos, M.S., Metaxa, Z.S. and Shah, S.P., 2010. Highly dispersed carbon
- nanotube reinforced cement based materials. Cement and Concrete Research, 40 (7), pp. 1052-
- 595 1059.
- 596 [24] Konsta-Gdoutos, M.S., Metaxa, Z.S. and Shah, S.P., 2010. Multi-scale mechanical and
- 597 fracture characteristics and early-age strain capacity of high performance carbon
- nanotube/cement nanocomposites. Cement and Concrete Composites, 32 (2), pp. 110-115.
- 599 [25] Metaxa, Z.S., Seo, J.W.T., Konsta-Gdoutos, M.S., Hersam, M.C. and Shah, S.P., 2012.
- 600 Highly concentrated carbon nanotube admixture for nano-fiber reinforced cementitious
- materials. Cement and Concrete Composites, 34 (5), pp. 612-617.
- [26] Saha, M., Tambe, P., Pal, S., Kubade, P., Manivasagam, G., Anthony Xavior, M. and
- 603 Umashankar, V., 2015. Effect of non-ionic surfactant assisted modification of hexagonal boron
- nitride nanoplatelets on the mechanical and thermal properties of epoxy nanocomposites.
- 605 Composite Interfaces, 22(7), pp. 611-627.
- Bhattacharjee, S., 2016. DLS and zeta potential—what they are and what they are not?.
- Journal of controlled release, 235, pp. 337-351.
- Danoglidis, P.A., Konsta-Gdoutos, M.S., Gdoutos, E.E. and Shah, S.P., 2016. Strength,
- energy absorption capability and self-sensing properties of multifunctional carbon nanotube
- reinforced mortars. Construction and Building Materials, 120, pp. 265-274
- [29] ACI PRC-544.1R-96: Report on Fiber Reinforced Concrete (Reapproved 2009)
- 612 [30] RILEM 50-FMC Committee (Fracture Mechanics of Concrete), 'Determination of the
- fracture energy of mortar and concrete by means of three-point bend tests on notched beams',
- 614 Mater. Struct. 18(106) (1985) 285–290.

- 615 [31] Griffin, A., Harvey, A., Cunningham, B., Scullion, D., Tian, T., Shih, C.J., Gruening,
- M., Donegan, J.F., Santos, E.J., Backes, C. and Coleman, J.N., 2018. Spectroscopic size and
- 617 thickness metrics for liquid-exfoliated h-BN. Chemistry of Materials, 30 (6), pp. 1998-2005
- 618 [32] Kong, D., Zhang, D., Guo, H., Zhao, J., Wang, Z., Hu, H., Xu, J. and Fu, C., 2019.
- 619 Functionalized boron nitride nanosheets/poly (L-lactide) nanocomposites and their
- 620 crystallization behavior. Polymers, 11 (3), p. 440.
- 621 [33] Andujar, J.L., Bertran, E. and Polo, M.C., 1998. Plasma-enhanced chemical vapor
- deposition of boron nitride thin films from B 2 H 6–H 2–NH 3 and B 2 H 6–N 2 gas mixtures.
- Journal of Vacuum Science & Technology A: Vacuum, Surfaces, and Films, 16 (2), pp. 578-
- 624 586.
- 625 [34] Zhang, B., Wu, Q., Yu, H., Bulin, C., Sun, H., Li, R., Ge, X. and Xing, R., 2017. High-
- efficient liquid exfoliation of boron nitride nanosheets using aqueous solution of alkanolamine.
- Nanoscale research letters, 12 (1), pp. 1-7.
- 628 [35] Lin, Y., Williams, T.V., Xu, T.B., Cao, W., Elsayed-Ali, H.E. and Connell, J.W., 2011.
- Aqueous dispersions of few-layered and monolayered hexagonal boron nitride nanosheets from
- sonication-assisted hydrolysis: critical role of water. The Journal of Physical Chemistry C, 115
- 631 (6), pp. 2679-2685.
- 632 [36] Coleman, J.N., 2009. Liquid-phase exfoliation of nanotubes and graphene. Advanced
- 633 Functional Materials, 19 (23), pp. 3680-3695.
- 634 [37] Zhang, W., Han, B., Yu, X., Ruan, Y. and Ou, J., 2018. Nano boron nitride modified
- reactive powder concrete. Construction and Building Materials, 179, pp.186-197.

- 636 [38] Scrivener, K.L., Juilland, P. and Monteiro, P.J., 2015. Advances in understanding
- hydration of Portland cement. Cement and Concrete Research, 78, pp. 38-56.
- 638 [39] Konsta-Gdoutos, M.S., Danoglidis, P.A., Falara, M.G. and Nitodas, S.F., 2017. Fresh and
- 639 mechanical properties, and strain sensing of nanomodified cement mortars: The effects of
- 640 MWCNT aspect ratio, density and functionalization. Cement and Concrete Composites, 82,
- 641 pp.137-151.
- 642 [40] Pan, Z., He, L., Qiu, L., Korayem, A.H., Li, G., Zhu, J.W., Collins, F., Li, D., Duan,
- W.H. and Wang, M.C., 2015. Mechanical properties and microstructure of a graphene oxide-
- cement composite. Cement and Concrete Composites, 58, pp. 140-147.
- [41] Liu, J., Jian, W. and Lau, D., 2022. Boron nitride nanosheet as a promising reinforcement
- 646 for cementitious composites. Applied Surface Science, 572, p.151395.
- [42] Liu, J., Hu, N., Chow, C.L. and Lau, D., 2022. Unfolding behavior of self-folded boron
- 648 nitride nanosheets inducing ductility of cementitious composites. Applied Surface Science,
- 649 599, p.153818.
- 650 [43] Li, C., Bando, Y., Zhi, C., Huang, Y. and Golberg, D., 2009. Thickness-dependent bending
- modulus of hexagonal boron nitride nanosheets. Nanotechnology, 20(38), p.385707.
- 652 [44] Liu, J., Li, Y., Jin, C., Lin, H. and Li, H., 2022. Effect and mechanism analysis of
- 653 hydroxylated nano-boron nitride on workability and multi-scale mechanical properties of
- cement paste. Archives of Civil and Mechanical Engineering, 22, 122.

- 656 [45] Li, Y., Wang, Y., Lv, Q., Qin, Z. and Liu, X., 2013. Synthesis of uniform plate-like boron
- nitride nanoparticles from boron oxide by ball milling and annealing process. Materials Letters,
- 658 108, pp. 96-102.
- 659 [46] Xie, K.Y., Domnich, V., Farbaniec, L., Chen, B., Kuwelkar, K., Ma, L., McCauley, J.W.,
- Haber, R.A., Ramesh, K.T., Chen, M. and Hemker, K.J., 2017. Microstructural characterization
- of boron-rich boron carbide. Acta Materialia, 136, pp. 202-214.

Doc	laration	of inte	rocte
1166	iaraiinn	m ini	312416

☑ The authors declare that they have no known competing financial interests or personal relationships that could have appeared to influence the work reported in this paper.
\Box The authors declare the following financial interests/personal relationships which may be considered as potential competing interests:

John Reight Cook